Morales Martinez, S.; Naranjo Ornedo, V.; Angulo Lopez, J.; Alcañiz Raya, ML. (2013). Automatic Detection of Optic Disc Based on PCA and Mathematical Morphology. IEEE Transactions on Medical Imaging. 32(4):786-796. doi:10.1109/TMI.2013.2238244.

Automatic detection of optic disc based on PCA and mathematical morphology

Sandra Morales, Valery Naranjo, Jesús Angulo, and Mariano Alcañiz

***Abstract*—The algorithm proposed in this paper allows to automatically segment the optic disc from a fundus image. The goal is to facilitate the early detection of certain pathologies and to fully automate the process so as to avoid specialist intervention. The method proposed for the extraction of the optic disc contour is mainly based on mathematical morphology along with principal component analysis (PCA). It makes use of different operations such as generalized distance function (GDF), a variant of the watershed transformation, the stochastic watershed, and geodesic transformations. The input of the segmentation method is obtained through PCA. The purpose of using PCA is to achieve the grey-scale image that better represents the original RGB image. The implemented algorithm has been validated on 5 public databases obtaining promising results. The average values obtained (a Jaccard's and Dice's coefficients of 0.8200 and 0.8932, respectively, an accuracy of 0.9947, and a true positive and false positive fractions of 0.9275 and 0.0036) demonstrate that this method is a robust tool for the automatic segmentation of the optic disc. Moreover, it is fairly reliable since it works properly on databases with a large degree of variability and improves the results of other state-of-the-art methods.**

***Index Terms*—Optic disc, principal component analysis, generalized distance function, watershed transformation, geodesic transformation.**

I. Introduction

DIABETIC retinopathy, hypertension, glaucoma and macular degeneration are nowadays some of the most common causes of visual impairment and blindness [1], [2]. Early diagnosis and appropriate referral for treatment of these diseases can prevent visual loss. Usually, more than 80% of global visual impairment is avoidable [2], and in the case of diabetes by up to 98% [3]. All of these diseases can be detected through a direct and regular ophthalmologic examination of the risk population. However, population growth, aging, physical inactivity and rising levels of obesity are contributing factors to the increase of them, which causes the number of ophthalmologists needed for evaluation by direct examination is a limiting factor. So, a system for automatic recognition of the characteristic patterns of these pathological cases would provide a great benefit. Regarding this aspect, optic disc (OD) segmentation is a key process in many algorithms designed for the automatic extraction of anatomical ocular structures, the detection of retinal lesions, and the identification of other fundus features. First, the OD location helps to avoid false positives in the detection of exudates associated with diabetic retinopathy, since both of them are spots with similar intensity [4]. Secondly, the OD margin can be used for establishing standard and concentric areas in which retinal vessel diameter measurements are performed by calculating some important diagnostic indexes for hypertensive retinopathy, such as central retinal artery equivalent (CRAE) and central vein equivalent (CRVE) [5], [6]. Thirdly, the relation between the size of the OD and the cup (cup-disc-ratio) has been widely utilized for glaucoma diagnosis [7], [8]. In addition, the relatively constant distance between the OD and the fovea is useful for estimating the location of the macula, area of the retina related to fine vision [9]. Moreover, the center, or even the border, of the OD also serves as initial point for vessel tracking algorithms due to the fact that all retinal vessels are originated from there [10].

Numerous OD segmentation methods, i.e. OD-boundary detectors, have been reported in the literature. In general, the presented techniques can mainly be grouped into template-based methods, deformable models, and morphological algorithms. Different approaches have been proposed according to template-based methods: edge detection techniques followed by the Circular Hough Transform [11], [12]; pyramidal decomposition and Hausdorff-based template matching [13]; colour decorralated templates [14]; or a kNN-regressor along with a circular template [9]. Concerning deformable models, GVF-snake [15], ASM [16], and modified active contours, which exploit specific features of the optic disc anatomy [17] or incorpore knowledge-based clustering and updating [18], have also been used to this purpose. As for algorithms based on mathematical morphology, most of them detect the OD by means of watershed transformation, generally through marker-controlled watershed [4], [19], [20], although each author chooses different markers. The centroid of the largest and brightest object of the image is consider as an approximation for the locus of the OD and it is used as internal marker [4]. The extended minima transformation [21] is applied to select the internal markers and external markers are calculated as an effectively partition of the image into regions, so that each region contains single internal marker and part of the background [19]. A list of pixels belonging to the main vessels arcade in the vicinity of an internal OD point previously detected are employed in [20]. On the other hand, some

Manuscript received January 3, 2013.

S. Morales, V. Naranjo, and M. Alcañiz are with the Instituto Interuniversitario de Investigación en Bioingeniería y Tecnología Orientada al Ser Humano, Universitat Politècnica de València, I3BH/LabHuman, Camino de Vera s/n, 46022 Valencia, Spain. E-mail: {smorales, vnaranjo, malcaniz}@labhuman.i3bh.es.

M. Alcañiz is also with Ciber, Fisiopatología de Obesidad y Nutrición, CB06/03 Instituto de Salud Carlos III, Spain.

J. Angulo is with Centre de Morphologie Mathématique, Mathématiques et Systèmes, MINES Paristech, France. E.mail: jesus.angulo@mines-paristech.fr

authors propose combining various algorithms to get a better approximation of the OD-boundary [22], [23].

Other methods related to the OD are focused on locating its center. On the whole, they are based on that all retinal vessels originate from the OD and their path follows a parabolic pattern [24]–[26].

The method proposed in this paper is mainly based on mathematical morphology although includes a principal component analysis (PCA) in the pre-processing stage. The main steps of the method are the following: First, the PCA is applied on the RGB fundus image in order to obtain a grey image in which the different structures of the retina, such as vessels and OD, are differentiated more clearly to get a more accurate detection of the OD. This stage is very important since it largely determines the final result. Then, the vessels are removed through inpainting technique to make the segmentation task easier. Next, a variant of the watershed transformation, the stochastic watershed transformation, followed to a stratified watershed, are implemented on a region of the original image. Finally, it must be discriminated which of the obtained watershed regions belong to the optic disc and which ones are not. A geodesic transformation and a further threshold are used to achieve that purpose.

The algorithm is fully automatic, so process is speeded up and user intervention is avoided making it completely transparent. Moreover, the method provides robustness in each processing step. First, it is independent of the database thanks to using PCA. Secondly, it employs the grey-image centroid as initial seed so that not only the pixel intensity is taken into account. Thirdly, it makes use of the stochastic watershed in order to avoid sub-segmentation problems related to classical watershed transformation. In addition to that, the proposed algorithm has produced state-of-the-art results in standard databases.

The rest of the paper is organized as follows: in Section II the main stages of the proposed method are described, including the principal component analysis, the inpainting technique performed as well as the segmentation algorithm. Section III shows the experimental results, the validation obtained using public databases, and a comparison with other methods from the literature. Finally, Section IV provides discussion and Section V conclusions and some future work lines.

II. Method

A. Theoretical background

1) *Principal Component Analysis*

The central idea of principal component analysis (PCA) is to reduce the dimensionality of a data set consisting of a number of interrelated variables, while retaining as much as possible of the variation present in the data set. This is achieved by transforming to a new set of variables, the principal components (PCs), which are uncorrelated, and ordered so that the first few retain most of the variations present in all of the original variables [27].

Suppose that $\mathbf{v}$ is a vector of p random variables, the kth PC, z_k, will be a linear function $\boldsymbol{\alpha}_k{}'\mathbf{v}$ of the elements of $\mathbf{v}$ where $\boldsymbol{\alpha}_k$ is a vector of p constants α_{k_1}, α_{k_2}, ..., α_{k_p} and $'$ denotes transpose

$$z_k = \boldsymbol{\alpha}_k{}'\mathbf{v} = \alpha_{k_1}v_1 + \alpha_{k_2}v_2 + ... + \alpha_{k_p}v_p = \sum_{j=0}^{p} \alpha_{k_j}v_j. \quad (1)$$

So that, $\boldsymbol{\alpha}_1{}'\mathbf{v}$ will have maximum variance, $\boldsymbol{\alpha}_2{}'\mathbf{v}$ will be uncorrelated with $\boldsymbol{\alpha}_1{}'\mathbf{v}$ and will have maximum variance, and so on, so that at the kth stage $\boldsymbol{\alpha}_k{}'\mathbf{v}$ will have maximum variance subject to being uncorrelated with $\boldsymbol{\alpha}_1{}'\mathbf{v}$, $\boldsymbol{\alpha}_2{}'\mathbf{v}$, ..., $\boldsymbol{\alpha}_{k-1}{}'\mathbf{v}$.

For a three-channel image transforming to a principal component space creates three new channels in which the first (the most significant) contains the most structural contrast and information. The rank for each axis in the principal set represents the significance of that axis as defined by the variance in the data along that axis. Thus, the first principal axis is the one with the greatest amount of scatter in the data and consequently the greatest amount of contrast and information, while the last principal axis represents the least amount of information such as noise and image artefacts [28]. In this case, the PCs are given by

$$z_k = \boldsymbol{\alpha}_k{}'\mathbf{f} = \alpha_{k_R}f_R + \alpha_{k_G}f_G + \alpha_{k_B}f_B, \quad (2)$$

where $\mathbf{f}(\mathbf{x}) = (f_R(\mathbf{x}), f_G(\mathbf{x}), f_B(\mathbf{x}))$ represents a RGB image and $k \in \{1, 2, 3\}$.

Specifically, principal-component axes ($\boldsymbol{\alpha}_k$) will be the eigenvectors of the covariance matrix $\boldsymbol{\Sigma}$. This is the matrix whose (i, j)th element is the covariance between the ith and jth elements of $\mathbf{f}$ when $i \neq j$, and the variance of the jth element of $\mathbf{f}$ when $i = j$ according to

$$\boldsymbol{\Sigma} = \begin{pmatrix} \sigma_R^2 & \sigma_{RG} & \sigma_{RB} \\ \sigma_{GB} & \sigma_G^2 & \sigma_{GB} \\ \sigma_{RB} & \sigma_{GB} & \sigma_B^2 \end{pmatrix}. \quad (3)$$

Being:

$$\sigma_{mn} = \frac{1}{N}\sum_{i=1}^{N}(f_{mi} - \bar{f}_m)(f_{ni} - \bar{f}_n), \quad (4)$$

where N is the number of pixels of the image, (m, n) represent the possible combinations between the RGB components and $\bar{f}_m$ and $\bar{f}_n$ determine the mean of the corresponding component, respectively.

Therefore, z_1, z_2, and z_3 are the PCs of the image $\mathbf{f}$ so that $\boldsymbol{\alpha}_1$ is the eigenvector corresponding to the largest eigenvalue of $\boldsymbol{\Sigma}$, $\boldsymbol{\alpha}_2$ corresponding to the second largest eigenvalue, and $\boldsymbol{\alpha}_3$ corresponding to the smallest one. Fig. 1 shows the PCs of a RGB fundus image where can be appreciated that the first PC contains the most structural contrast and information.

2) *Inpainting*

Inpainting algorithms are used in diverse applications, from the restoration of damaged photographs to the removal/replacement of selected objects [29]. These algorithms usually try to fill selected parts of an image by propagating external information so that structure continuity is preserved.

Let a binary image $\Omega(\mathbf{x})$ stand for the region to be inpainted and $\partial\Omega$ for its boundary. For each $\partial\Omega$-pixel, $\mathbf{x}$, the inpainted-pixel value is computed as

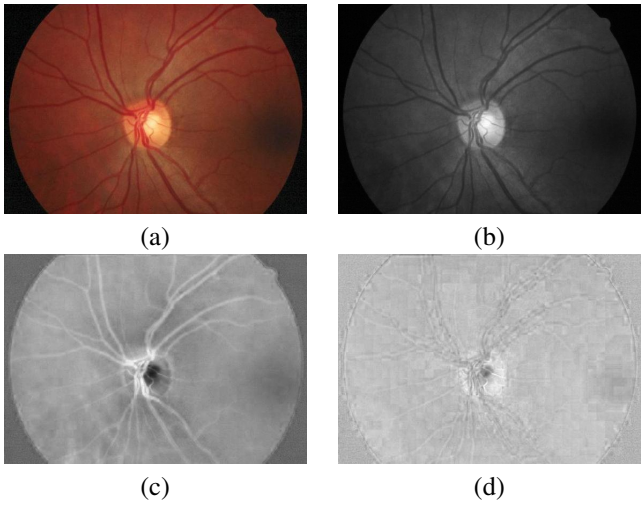

Fig. 1. Principal components (PCs): (a) Original fundus image, (b) First PC z_1, (c) : Second PC z_2 and (d) Third PC z_3.

$$P(\mathbf{x}) = \frac{\sum_{k=1}^{n} \frac{P_k(\mathbf{x})}{l_k}}{\sum_{k=1}^{n} \frac{1}{l_k}}, \tag{5}$$

where P_k denotes the pixel values in a 5 x 5 neighbourhood of the pixel under consideration, n is the number of neighbouring pixels, and l_k is the distance between the pixel $\mathbf{x}$ and each neighbouring pixel. So that, the inpainted image $\Upsilon(f,\Omega)(\mathbf{x})$ of a gray image $f(\mathbf{x})$ is

$$\Upsilon(f,\Omega)(\mathbf{x}) = \begin{cases} f(\mathbf{x}) & \text{if } \partial\Omega(\mathbf{x}) = 0 \\ P(\mathbf{x}) & \text{if } \partial\Omega(\mathbf{x}) = 255. \end{cases} \tag{6}$$

After filling $\partial\Omega$ with the computed values, the $\partial\Omega$-pixels are removing from Ω and $\partial\Omega$ is recalculated. The process is repeated until the mask is empty and all pixels have been filled.

*3) **Morphological operators***

Mathematical morphology is a non-linear image processing methodology based on minimum and maximum operations [30] whose aim is to extract relevant structures of an image.

Let f be a grayscale image which is defined as $f(\mathbf{x}) : E \rightarrow T$ where $\mathbf{x}$ is the pixel position. In the case of discrete valued images, $T = \{t_{min}, t_{min}+1, ..., t_{max}\}$ is an ordered set of gray-levels. Typically, in digital 8-bit images $t_{min} = 0$ and $t_{max} = 255$. Furthermore, let $B(\mathbf{x})$ be a sub-set of Z^2 called structuring element (shape probe) centered at point $\mathbf{x}$, whose shape is usually chosen according to some a priori knowledge about the geometry of the relevant and irrelevant image structures. The two basic morphological operators are:

$$\begin{aligned} &Dilation : [\delta_B(f)](\mathbf{x}) = \max_{b\in B(\mathbf{x})} f(\mathbf{x}+\mathbf{b}) \\ &Erosion : [\varepsilon_B(f)](\mathbf{x}) = \min_{b\in B(\mathbf{x})} f(\mathbf{x}+\mathbf{b}). \end{aligned} \tag{7}$$

Their purpose is to expand light or dark regions, respectively, according to the size and shape of the structuring element. Those elementary operations can be combined to obtain a new set of operators or basic filters given by:

$$\begin{aligned} &Opening : \gamma_B(f) = \delta_B(\varepsilon_B(f)) \\ &Closing : \varphi_B(f) = \varepsilon_B(\delta_B(f)). \end{aligned} \tag{8}$$

Light or dark structures are respectively filtered out from the image by these operators regarding the structuring element chosen.

Other morphological operators that complement the previous ones are geodesic transformations. The *geodesic dilation* is the iterative unitary dilation of an image f (marker) which is contained within an image g (reference),

$$\delta_g^{(n)}(f) = \delta_g^{(1)}\delta_g^{(n-1)}(f), \text{ being } \delta_g^{(1)}(f) = \delta_B(f) \wedge g. \tag{9}$$

The *reconstruction by dilation* is the successive geodesic dilation of f regarding g up to idempotence,

$$\gamma^{rec}(g,f) = \delta_g^{(i)}(f), \text{ so that } \delta_g^{(i)}(f) = \delta_g^{(i+1)}(f). \tag{10}$$

Using the *geodesic reconstruction*, a *close-hole operator* can also be defined. For a grey-scale image, it is considered a hole any set of connected points surrounded by connected components of value strictly greater than the hole values. This operator fills all holes in an image f that do not touch the image boundary f_∂ (used as marker):

$$\psi^{ch}(f) = [\gamma^{rec}(f^c, f_\partial)]^c, \tag{11}$$

where f^c is the complement image (i.e., the negative).

*4) **Grey-image centroid***

The centroid of a grey-level image can be calculated based on the generalized distance function (GDF) [31]. This algorithm is focused on modifying the classic two-pass sequential distance function [32] so that: (1) edge cost is taken into account; (2) raster and anti-raster scans of the image are iterated until stability. Let be $N^+(p)$ (resp., $N^-(p)$) the 8-connected neighbourhood of pixel p scanned before p (resp., after p) in a raster scan, and $C_f(p,q) = f(p) + f(q)$ the associated cost to two neighbouring pixels p and q, the algorithm of GDF to set X in an image f proceeds as follows:

- Initialise result image d_f : $d_f(p) = 0$ if $p \in X$ and $d_f(p) = +\infty$ otherwise.
- Iterate until stability, for each pixel p:
  - Scan image in raster order: $d_f(p) \leftarrow min\{d_f(p), min\{d_f(q) + C_f(p,q), q \in N^+(p)\}\}$.
  - Scan image in anti-raster order: $d_f(p) \leftarrow min\{d_f(p), min\{d_f(q) + C_f(p,q), q \in N^-(p)\}\}$.

More specifically, the grey-level centroid of an image f can be obtained as the maximum of the GDF to the image border set B as follows:

- Compute GDF to set B in image f, $d_f(B)$.
- Find the maximal value of $d_f(B)$, u_{max}.
- Threshold $d_f(B)$ with the u_{max} calculated to define set C as image centroid.

- If C has more than one pixel, compute the centroid of set C as the maximum edge distance.

*5) **Stochastic watershed transformation***

Watershed transformation [33] is a segmentation technique for gray-scale images. This algorithm is a powerful segmentation tool whenever the minima of the image represent the objects of interest and the maxima are the separation boundaries between objects. Due to this fact, the input image of this method is usually a gradient image. In mathematical morphology, the gradient $\varrho(f)(\mathbf{x})$ of an image $f(\mathbf{x})$ is obtained as the pointwise difference between a unitary dilation and a unitary erosion, i.e.,

$$\varrho(f)(\mathbf{x}) = \delta_B(f)(\mathbf{x}) - \varepsilon_B(f)(\mathbf{x}). \tag{12}$$

In the case of a gradient image is considered as input image, the watershed transformation produces a segmentation which can be viewed as: a set of closed contours of segmented regions which will be noted by $WS(\varrho(f))$, or a partition of the space E in a set of classes named $\Pi(WS(\varrho(f)))$.

However, one problem of this technique is the over-segmentation, which is caused by the existence of numerous local minima in the image normally due to the presence of noise. One solution to this problem is using marker-controlled watershed, $WS(\varrho)_{f_{mrk}}$, in which the markers f_{mrk} artificially indicate the minima of the image. Nevertheless the controversial issue consists in determining f_{mrk} for each region of interest,

$$f_{mrk}(\mathbf{x}) = \begin{cases} 0 & \text{if } \mathbf{x} \in marker \\ 255 & Otherwise. \end{cases} \tag{13}$$

Note that the use of few markers along with the existence of borders within the OD can also cause that some parts of it are not detected (sub-segmentation). So that, the choice of the correct markers is crucial for the effectiveness and robustness of the algorithm.

A watershed transformation variant is used to solve this conflict, the stochastic watershed [34]. In this transformation, a given number M of marker-controlled-watershed realizations are performed selecting N random markers in order to estimate a probability density function (*pdf*) of image contours and filter out non significant fluctuations. Let $\{f_{mrki}\}_{i=1}^{M}$ be M sets of N uniform random markers and $WS_i = WS(\varrho)_{f_{mrki}}$ the ith output image of the marker-controlled watershed imposed by f_{mrki}. The *pdf* of image contours is computed by Parzen window method [35] as follows

$$pdf(\mathbf{x}) = \frac{1}{M}\sum_{i=1}^{M}(WS_i(\mathbf{x}) * G(\mathbf{x}; s)), \tag{14}$$

where $G(\mathbf{x}; s)$ represents a Gaussian kernel of variance σ^2 and mean μ ($\mu = 0$)

$$G(\mathbf{x}; s) = \frac{1}{2\pi\sigma^2} e^{-\left(\frac{\|\mathbf{x}\|^2}{2\sigma^2}\right)}. \tag{15}$$

Afterwards, it is necessary to perform a last marker-controlled watershed on the *pdf* obtained.

This type of watershed works better than other marker-based watershed transformations used previously in the literature. In the next section it will be explained in detail.

B. Algorithm

The automatic OD-segmentation method proposed in this paper is focused on using different operations based on mathematical morphology on a fundus image to obtain the OD-contour. Previously, a pre-processing of the original RGB image is required. The first step of the pre-processing consists of applying PCA to transform the input image to grey scale. This technique combines the most significant information of the three components RGB in a single image so that it is a more appropriate input to the segmentation method. After segmentation, a post-processing is also performed to fit the final region contour by a circumference. In Fig. 2, the block diagram of the complete segmentation process is depicted.

*1) **Pre-processing***

- *PCA*

Generally, an initial gray-scale image is necessary to carry out most of the segmentation algorithms of the literature. However, in the case of the OD segmentation, each author considers appropriate a different intensity image, such as a band of the original RGB image [4], [9] or a component of other color spaces [15], [17]. In this work, the use of a new grey-scale image is proposed. Specifically, it is calculated by means of PCA because this type of analysis maximizes the separation of the different objects that compose a image so that the structures of the retina are better appreciated. In addition, it is much less sensitive to the existing variability in a fundus image regarding color, intensity, etc. As seen in section II-A1, the first PC is the most significant so, z_1, defined as equation (2), is chosen as the input image of the method presented in this paper. It must be stressed that to ensure that z_1 contains the most structural contrast and information of the original RGB channels, it should be verified that the largest eigenvalue represents at least a 90% of the total sum of eigenvalues. In spite of this situation is not often in the consulted databases, if the largest eigenvalue represents less than 90%, the components whose sum of eigenvalues get the 90% must be processed in parallel. Afterwards, the input of the watershed transformation will be the pixel-wise maximum of the gradient images.

- *Image enhancement*

The non-uniform illumination of this grey image is also corrected and its contrast is increased through a local transformation (Γ). The transformation for shade correction is given by the expression

$$\Gamma(f)(t) = \begin{cases} \frac{\frac{1}{2}(u_{max}-u_{min})}{(\mu_f - t_{min})^r}(t - t_{min})^r + u_{min} & \text{if } t \le \mu_f \\ \frac{-\frac{1}{2}(u_{max}-u_{min})}{(\mu_f - t_{max})^r}(t - t_{max})^r + u_{max} & \text{if } t > \mu_f. \end{cases} \tag{16}$$

where t_{min} and t_{max} are the minimum and maximum grey level of the image respectively, u_{min} and u_{max} are the target levels (typically 0 and 255 respectively), μ_f is the mean

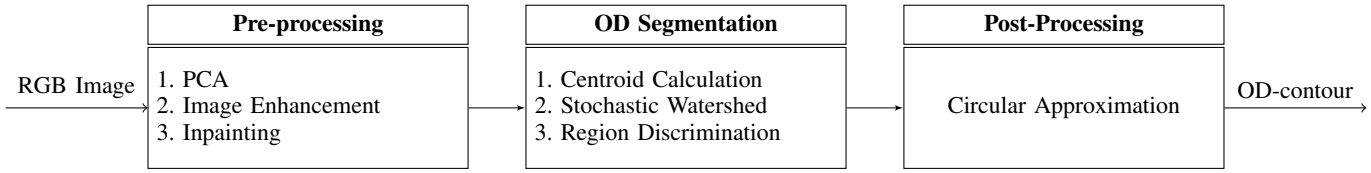

Fig. 2. Optic disc segmentation diagram.

value of the image for all pixels within a window centred at the current pixel $\mathbf{x}$ and with a size larger than the OD, and the parameter r is used to control the contrast increasing (experimentally $r = 2$). Γ is applied on z_1 resulting an enhanced image

$$z_1^{'} = \Gamma(z_1)(t). \tag{17}$$

- *Inpainting*

Retinal vessels are originated from the OD therefore there are numerous vessels crossing its border which makes its discrimination difficult. So, vessel removal of the enhanced image is implemented by the inpainting technique explained in section II-A2,

$$z_1^{''} = \Upsilon(z_1^{'}, \Omega). \tag{18}$$

Its aim is to extract the OD-boundary more precisely and to reduce the existing borders within the OD which increase the risk of sub-segmentation.

In particular, the region to be inpainted Ω is a binary mask of the retinal vessels, which must have been segmented previously. Hence, a rough segmentation of the vessels is performed by means of a k-means clustering [36] from the green band of the original image with a k value equals to 3. This algorithm classifies the image pixels in 3 clusters so that each pixel belongs to the cluster with the nearest mean. Then, two of the three obtained clusters are defined as vessel. Three classes are required because thick and thin vessels may be very different. Afterwards, a unitary morphological dilation of the segmented vessels yields the final vessel mask. The purpose of this operation is to make sure that the vessels will be contained in the mask.

In Fig. 3 the performed pre-processing of the original image, shown in Fig. 1(a), can be observed, both the obtaining of the first PC and its enhancement by means of non-linear transformation Γ and also the vessel removal. Note that the whole image is processed although only a region of interest is shown for better visualisation.

*2) **OD Segmentation***

- *Stochastic watershed transformation*

As mentioned above, the segmentation method makes use of the stochastic watershed. This transformation uses random markers to build a probability density function (*pdf*) of contours, according to equation 14, which is then segmented by volumic watershed for defining the most significant regions. However, in the marker definition not only internal markers (that specify what is the object of interest) are needed, but also an external marker which limits the area to be segmented.

On the one hand, the chosen external marker, f_{ext}, will be a circle of constant diameter centred on the centroid of the image, calculated as section II-A4. Specifically, the size of this circle is related to the image size, so that it is approximated by a 15% of the size of the fundus image (with this size we made sure that the optic disc is included). This way for calculating the grey-image centroid combines the centrality of the image with respect to edge distance (i.e. purely geometric) but penalizing this distance in relation to the intensities. Thus, note that it can not be defined as the center of mass of the intensities or as the center of the brighter and larger zone, since the two effects are combined. For that reason, to use this algorithm to calculate the centroid of a retinal image, it must be made sure that the optic disc is a brighter zone than the background (sufficiently contrasted) and it has a significant size with respect to the image size. So, it is advisable to compute this algorithm on the residue of a close holes of the original grey image. In Fig.4 the different results of the algorithm can be appreciated, both applied to the first principal component of the original image after inpainting technique and applied to the residue of a close holes of the previous image.

On the other hand, the internal markers, f_{int}, will be uniform random markers generated within the area limited by f_{ext}. Hence, the final set of markers (external and internal), f_m is the logical OR of both of them,

$$f_m = f_{int} \vee f_{ext}. \tag{19}$$

In particular, the *pdf* is built from 15 marker-controlled-watershed realizations, as showed in section II-A5, using as input the gradient of the inpainted image (Fig. 5(c)). Therefore, in that case, the ith watershed output $WS_i = WS(\varrho(z_1^{''}))_{f_{m_i}}$, being f_{m_i} the final set of markers used in the corresponding simulation. f_{int} is generated for each simulation while f_{ext} is the same in all of them. The number of internal markers used is $N = 100$. An example of f_m can be observed in Fig. 5(d).

Obtaining a *pdf* of the contours of the watershed regions (Fig. 5(e)) facilitates the final segmentation, providing robustness and reliability since the arbitrariness in choosing the markers is avoided. Afterwards, the *pdf* can be combined with the initial gradient in order to reinforce the gradient contours which have a high probability resulting a probabilistic gradient [34],

$$\rho(z_1^{''})(\mathbf{x}) = (1-\lambda)\varrho(z_1^{''})(\mathbf{x}) + \lambda pdf(\mathbf{x}), \tag{20}$$

with $\lambda = 0.5$ the results are in general satisfactory.

Finally, a last marker-controlled watershed is applied to $\rho(z_1^{''})(\mathbf{x})$ using a new set of markers $f_{m'}$, giving rise to the image $\Pi(WS(\rho(z_1^{''})_{f_{m'}}))$, which is shown in Fig. 5(g), where the different obtained regions can be appreciated. In this case, stratified markers are employed instead of random

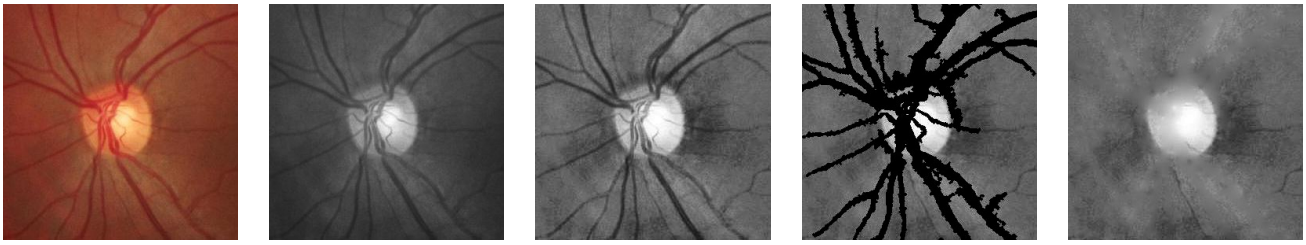

(a) (b) (c) (d) (e)

Fig. 3. Pre-processing: (a) Original image, (b) First PC z_1, (c) Enhanced image z_1', (d) Vessel mask to be inpainted Ω, and (e) Inpainted image z_1''.

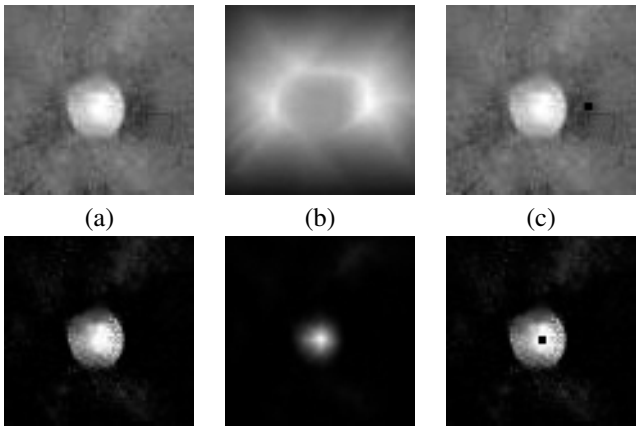

(a) (b) (c) (d) (e) (f)

Fig. 4. Grey-image centroid. (a) First PC (z_1) after inpainting technique, (b) GDF of (a), (c) Image centroid, (d) Residue of close operator of (a), (e) GDF of (d), and (f) Image centroid.

markers. Specifically, stratified markers are uniform markers generated within an area. The generation of stratified markers consists of dividing the region to be segmented into a uniform grid, and only the centroid of each region is considered as marker as shown Fig. 5(f). The reason for using this type of markers is to make sure that every pixel within the area in question belongs to a watershed region. Due to the fact that there are markers located outside the OD, not all regions obtained by the watershed transformation are wanted. If each region of $\Pi(WS(\rho(z_1^{''})_{f_{m'}}))$ is named as Π_i, the next stage of the proposed method is to discriminate which Π_i are significant and which ones are not and should be filtered out. Fig. 5 depicts all steps of the segmentation process: centroid computation, watershed transformation and the removing of the unwanted regions.

- *Region discrimination*

The discrimination between the significant and non-significant regions is based on the average intensity of the region. The value of each region will be equal to

$$\mu_{\Pi_i} = \frac{1}{N_i} \sum_{\mathbf{x} \epsilon \Pi_i} z_1^{''}(\mathbf{x}), \tag{21}$$

being N_i the number of pixels of the corresponding region Π_i. Fig. 5(h) represents the image μ_Π where the intensity of each region is equal to μ_{Π_i}. The regions belonging to the optic disc will be light regions around darker regions therefore the residue of a close-hole operator is calculated on μ_Π to obtain the regions that accomplish this condition (Fig. 5(i)). Afterwards, a threshold is applied on the resulting image to select the valid regions. This operation leads to the final OD segmentation (Fig. 5(j)). The value of the threshold is $u = m - 2s$, being m and s the mean and the standard deviation of the residue of the close-hole operator.

*3) **Post-processing***

Once the region of interest has been obtained, the result must be fitted to eliminate false contours, which are detected due generally to the blood vessels that pass through the OD. The inpainting technique was performed to remove most of them, as previously mentioned, however some irregularities can still be appreciated in the final region contour (Fig. 6(a)).

In this work, the OD-contour has been estimated as a circle in the same way that in [9], [12], [13] although a elliptical shape could also have been chosen. The main reason for fitting the OD by a circle is because this algorithm will later be used to establish a zone of the retina concentric to the OD-margin according to a standard protocol with the aim to perform vessel diameter measurements [37]. The fit is performed by means of Kasa's method [38] which lets calculate the center and the radius of the circle that better is adapted to a binary region through least squares. Fig. 6 shows the contour of the final region obtained by the proposed method and its circular approximation.

III. Results

The validation of the method has been carried out on 5 public databases: DRIONS [39], DIARETDB1 [40], DRIVE [41], MESSIDOR [42], and ONHSD [17], [43]. In DRIONS database 110 fundus images of 600 x 400 pixels with their OD manually segmented by two different specialists are included. The mean age of the patients was 53.0 years (S.D. 13.05), with 46.2% male and 53.8% female and all of them were Caucasian ethnicity. 23.1% patients had chronic simple glaucoma and 76.9% eye hypertension. Some of the 110 images contain visual characteristics related to potential problems that may distort the detection process of the OD-contour: light artefacts (3 images), some of rim blurred or missing (5 images), moderate peripapillary atrophy (16 images), concentric peripapillary atrophy/artefacts (20 images), and strong pallor distractor (6 images). DIARETDB1 database consists of 89 colour fundus images of size 1500 x 1152 pixeles. 84 of them contain at least mild non-proliferative signs (microaneurysms) of the diabetic

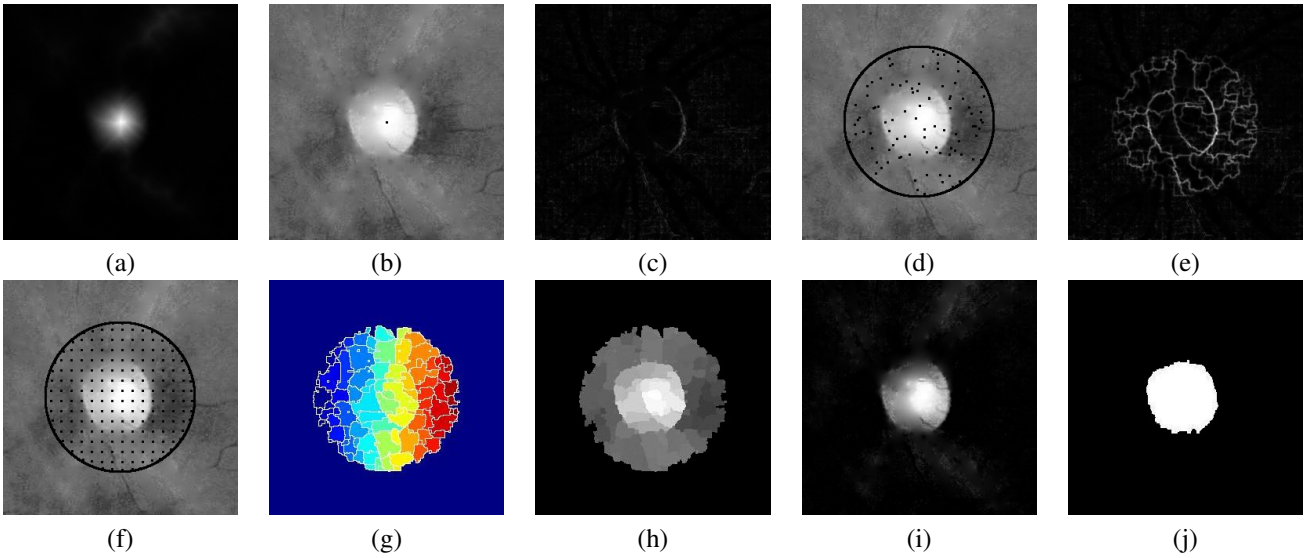

Fig. 5. OD Segmentation: (a) GDF, (b) Centroid image, (c) Gradient image $\varrho(z_1^{''})$, (d) Uniform random markers, (e) Probability density function of contours using 15 simulations and 100 internal markers, (f) Stratified markers, (g) Watershed regions $\Pi(WS(\rho(z_1^{''})_{f_{m'}}))$, (h) Average intensity of the watershed regions μ_Π, (h) Residue of close-hole operator, and (i) Thresholding.

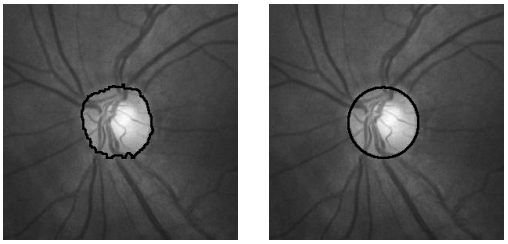

Fig. 6. Post-processing: (a) Contour of the obtained region, and (b) Circular approximation of the OD contour.

retinopathy, and 5 are considered as normal which do not contain any signs of the diabetic retinopathy according to all experts who participated in the evaluation. These images was resized to 750 x 576 pixels in order to save computation time. DRIVE database contains 40 retinal images of 565 x 584 pixels, 33 do not show any sign of diabetic retinopathy and 7 show signs of mild early diabetic retinopathy. MESSIDOR database, kindly provided by the Messidor program partners, contains 1200 eye fundus color images of the posterior pole. The images were captured using 8 bits per color plane at 1440 x 960, 2240 x 1488 or 2304 x 1536 pixels. 800 images were acquired with pupil dilation and 400 without dilation. For each image, two diagnosis have been provided: retinopathy grade and risk of macular edema. Finally, ONHSD dataset contains 99 fundal images with a resolution of 640 x 480 taken from 50 patients randomly sampled from a diabetic retinopathy screening programme; 96 images have discernable ONH. The subjects are from various ethnic backgrounds; 19 have type 2 diabetes mellitus, while the diabetes status was unavailable for the remaining 31. In this database there is considerable quality variation in the images, with many characteristics that can affect segmentation algorithms. The ONH centre has been marked up a clinician, and four clinicians marked the ONH edge where it intersects with radial spokes (at 15 degree angles) radiating from the nominated centre.

The performance of the method has been evaluated in based on different concepts. Jaccard's (JC) and Dice's (S) coefficients describe similarity degree between two compared elements being equal to 1 when segmentation is perfect. Accuracy (Ac) is determined by the sum of correctly classified pixels as OD and non-OD divided by the total number of pixels in the image. True positive fraction (TPF) is established by dividing the correctly classified pixels as OD by the total number of OD pixels in the gold standard. False positive fraction (FPF) is calculated by dividing the misclassified pixels as OD by the total number of non-OD pixels in the gold standard. Finally, in order to be able to compare with more other authors' works, another measure was calculated: the mean absolute distance (MAD) [44], whose aim is to measure the accuracy of the OD-boundary.

In Table I the results achieved on the 5 databases can be observed. On the one hand, in order to analyse the results on DRIONS database, the first observer images of this database have been taken as reference (gold standard) to calculate similarity degree between them and our segmentation. Regarding MESSIDOR database, the OD rim of these 1200 images has been hand segmented and it is currently available online to facilitate performance comparison between different methods [45]. Concerning ONHSD dataset, the average of the edges marked by the four experts has been used to generate the reference images. On the other hand, neither DIARETDB1 nor DRIVE database have the OD segmented publicly available. In those cases, we have compared our results with the same ground truth used in [20], where the contour of each image was labelled by four ophthalmologists, and then, only the mean of those contours is considered as ground truth.

As it was mentioned in section I, most OD segmentation

TABLE I
RESULTS (AVERAGE VALUES AND STANDARD DEVIATIONS) OBTAINED BY THE PROPOSED METHOD USING THE DRIONS, DIARETDB1, DRIVE, MESSIDOR, AND ONHSD DATABASES. JACCARD'S (JC) AND DICE'S (S) COEFFICIENTS, ACCURACY (AC), TRUE POSITIVE (TPF) AND TRUE NEGATIVE FRACTIONS (FPF), AND MEAN ABSOLUTE DISTANCE (MAD).

	DRIONS	DIARETDB1	DRIVE	MESSIDOR	ONHSD
JC	0.8424 (0.1174)	0.8173 (0.1308)	0.7163 (0.1880)	0.8228 (0.1384)	0.8045 (0.1175)
S	0.9084 (0.0982)	0.8930 (0.0913)	0.8169 (0.1712)	0.8950 (0.1056)	0.8867 (0.0776)
Ac	0.9934 (0.0051)	0.9957 (0.0039)	0.9903 (0.0134)	0.9949 (0.0050)	0.9941 (0.0042)
TPF	0.9281 (0.1177)	0.9224 (0.1058)	0.8544 (0.1938)	0.9300 (0.1239)	0.9310 (0.1046)
FPF	0.0040 (0.0041)	0.0028 (0.0029)	0.0061 (0.0085)	0.0035 (0.0041)	0.0043 (0.0042)
MAD	2.4945 (2.5139)	2.8786 (3.0285)	5.8538 (10.1797)	4.0759 (6.0909)	3.2753 (3.0407)

methods are divided into morphological algorithms, template-based methods, and deformable models. The proposed algorithm has been compared with several methods of each category. Most works have been selected due to the fact they use some of the analysed databases, and thereby, the current and future comparison is facilitated.

- *The presented method versus other morphological algorithms*

On the one hand, Table II is focused on analysing further DRIONS database at the same time that the performance of our work is contrasted with the performance of other method based on mathematical morphology. So, first, the segmented images by the second observer have also been compared with the gold standard to obtain inter-expert differences, and secondly, other existing technique based on marker-controlled-watershed transformation [4] has been implemented and compared with ours.

TABLE II
COMPARISON OF THE PARAMETERS OF TABLE I ACHIEVED BY THE PROPOSED METHOD, BY THE 2^{nd} OBSERVER AND BY OTHER MARKER-CONTROLLED-WATERSHED ALGORITHM ON DRIONS DATABASE.

	Proposed method	$2^{\mathbf{nd}}$ observer	Walter et al. [4]
JC	0.8424 (0.1174)	0.9202 (0.0455)	0.6227 (0.3695)
S	0.9084 (0.0982)	0.9578 (0.0265)	0.6813 (0.3854)
Ac	0.9934 (0.0051)	0.9970 (0.0017)	0.9689 (0.0492)
TPF	0.9281 (0.1177)	0.9498 (0.0537)	0.6715 (0.3980)
FPF	0.0040 (0.0041)	0.0012 (0.0009)	0.0210 (0.0417)
MAD	2.4945 (2.5139)	0.7408 (0.5483)	29.6289 (53.9186)

On the other hand, the concepts of Jaccard's coefficient (also known as area overlap) and the MAD included in Table I allow us to compare with the method proposed in [20] as well as with other state-of-the-art algorithms that were analysed in it. According to these data, our method obtains a mean overlap greater than 70% for the five databases which signifcantly improves the results of the compared methods inasmuch as the best results were around 40%. As for as the average MAD, our MAD values are the smallest in almost all cases analysed. In particular, Table III compares the results of our method with the method that achieved the best results in [20] and on the same databases (DIARETDB1 and DRIVE).

- *The presented method versus template-based methods*

The validation on MESSIDOR database has been performed through the comparison with a circular template-based method and four elliptical template-based approaches [12]. The methods analysed in this work can be compared in based on Jaccard's coefficient. Three of the elliptical template-based variants were based on minimizing the algebraic distance (achieving a $JC \simeq 0.66$), and one was based on minimizing the geometric distance ($JC = 0.67$). Our method improves the performance of all elliptical approaches and achieves comparable results with the circular template-based method ($JC = 0.86$).

- *The presented method versus deformable models*

Our method has also been tested on ONHSD database in order to compare with the tree approaches based on deformable models evaluated in [17]. In addition, with the aim of achieving a rigorous comparison, the same metric used in this work has been calculated. A subjective perception of quality, which is based on four categories, was defined as a way of classifying the performance. For that, they define the discrepancy δ^j as

$$\delta^j = \sum_i \frac{\mid m_i^j - \mu_i^j \mid}{\sigma_i^j + \epsilon}, \tag{22}$$

where μ_i^j and σ_i^j summarize the clinician's choice of rim location on spoke i of image j. Division by σ compensates for uncertainty in rim position; $\epsilon = 0.5$ is a small factor to prevent division by zero where the clinicians are in exact agreement. Each image is classified as *Excellent*, *Good*, *Fair*, or *Poor* depending on the discrepancy value (up to one, two, five, or more, respectively).

Table IV summarizes the performance of our method on the subjective classification of the ONHSD dataset so that it is directly comparable with the results presented in [17]. While the best approach of this work has Excellent-Fair performance in 83% of cases, our method obtains it in 94%.

In addition to the presented results, a correlation analysis through a scatterplot (Fig.7) was performed in order to assess the performance of image segmentation in depth. In particular, the correlation between the OD-area determined automatically and reference standard is shown. It can be observed that, in general, the points are close to the identity line. It should be noted that, with the aim of representing several databases with different resolutions in the same graph, the relative OD-area has been calculated normalizing by the total number of retinal pixels.

TABLE III
COMPARISON OF THE PROPOSED METHOD WITH THE WORK PRESENTED IN [20] IN BASED ON JACCARD'S COEFFICIENT (JC) AND MEAN ABSOLUTE DISTANCE (MAD) ON DIARETDB1 AND DRIVE DATABASES.

	DIARETDB1		DRIVE	
	Proposed method	**Welfer et al. [20]**	**Proposed method**	**Welfer et al. [20]**
JC	0.8173 (0.1308)	0.4365 (0.1091)	0.7163 (0.1880)	0.4147 (0.0833)
MAD	2.8786 (3.0285)	8.31 (4.05)	5.8538 (10.1797)	5.74

TABLE IV
SUBJECTIVE CLASSIFICATION OF PERFORMANCE ON ONHSD DATASET.

	Excellent	**Good**	**Fair**	**Poor**	**Excellent-Fair**
Proposed method	28%	36%	31%	6%	94%
TemploralLock [17]	42%	31%	10%	17%	83%
Simple [17]	9%	8%	30%	53%	47%
DV-Hough [17]	39%	22%	20%	19%	81%

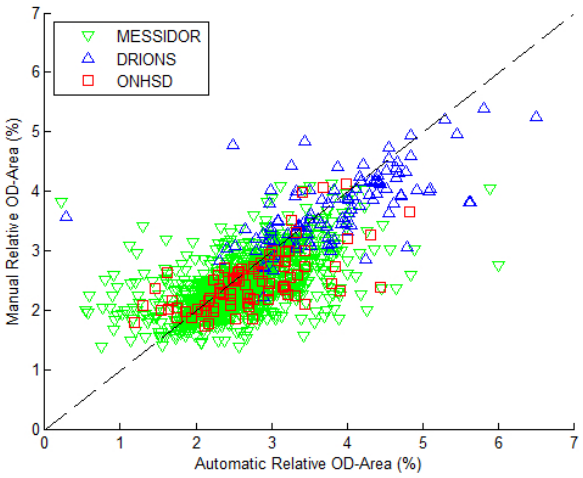

Fig. 7. Scatterplot of manual versus automatic segmentation of OD-area.

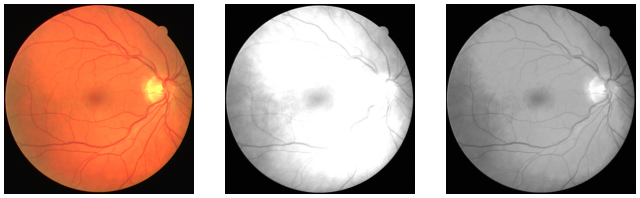

(a) (b) (c)

Fig. 8. Advantadges of PCA: (a) Original RGB fundus image, (b) Red component and (c) Image obtained by PCA.

TABLE V
COMPARISON BETWEEN THE USE OF PCA VERSUS THE USE OF THE RED COMPONENT ON DRIVE DATABASE.

	PCA	**Red Component**
JC	0.7163 (0.1880)	0.4106 (0.3926)
S	0.8169 (0.1712)	0.4674 (0.4256)
Ac	0.9903 (0.0134)	0.8979 (0.2044)
TPF	0.8544 (0.1938)	0.5607 (0.4368)
FPF	0.0061 (0.0085)	0.0994 (0.2343)
MAD	5.8538 (10.1797)	72.7412 (87.2160)

IV. DISCUSSION

Variability between fundus images in color, intensity, size, presence of artefacts, etc. makes each state-of-the-art method uses a different input image: green [9], [13], [19] and red [4], [20], [22] band of the original RGB image, or even a combination of both of them [12], [46], intensity component extracted from the HSI representation [17] and lightness channel of the HLS space [15]. However, due to this fundus image variability, they do not always provided the desired results. Therefore a PCA, able to maximize the separation between the different objects of the image, has been proposed in this paper as a more appropriate input image. For example, in Fig. 8, PCA is compared with the use of the red component on a specific image. It can be observed that while the red component is completely over-saturated, PCA obtains a grey image where the OD could be segmented. Specifically, in Table V a quantitative analysis about the use of those two color planes can be observed concluding that the employment of PCA improves the final results.

As for improvements achieved by the proposed method in relation to others which use watershed transformation must also be highlighted. In particular, the different steps of our method help to avoid sub-segmentation problems, as occurs in Fig. 9 where the original image has been segmented using only one internal marker located in the geodesic center of its largest and brightest object [4].

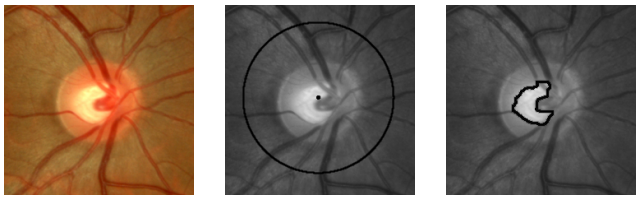

(a) (b) (c)

Fig. 9. Sub-segmentation problem produced in other marker-controlled-watershed method: (a) Original image, (b)Internal and external marker, and (c) Contour of watershed region.

Referring to the databases employed, most of the images included in them are pathological and therefore can distort

the OD detection. For example, the images of patients with diabetic retinopathy may contain exudates which are of similar intensity to the OD or patients with glaucoma can suffer from peripapillary atrophy. Concretely, Fig. 10 shows the robustness of the method in presence of exudates. However, if the lesion is as big as the optic disc and brighter, it is true that the method may fail.

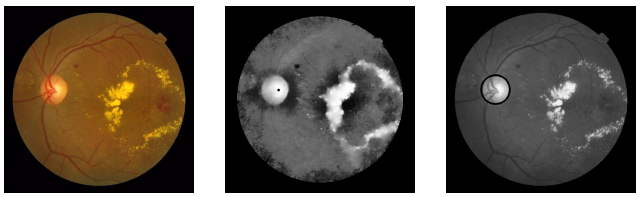

(a) (b) (c)

Fig. 10. Robustness of the grey-image centroid in presence of exudates: (a) Original image, (b) First PC (z_1) after inpainting technique with the centroid in black, and (d) Result of the proposed method.

In summary, the weighted average of the results (according to the number of images of each database) are: JC=0.8200, S=0.8932, Ac=0.9947, TPF=0.9275, FPF=0.0036, and MAD=3.8883. Note that our method is fairly reliable since it works properly on databases with a large degree of variability and improves the results of other state-of-the-art methods. Moreover, it must be taken into account that all used databases are public and, therefore, it will be easier carrying out future comparisons.

Due to the complexity of the fundus images, their high number of elements makes a perfect segmentation difficult. That is the reason for which a circular approximation is applied on the segmented disc.

V. Conclusions

In this paper a new approach for the automatic detection of the optic disc has been presented. First, it is focused on the use of a new grey image as input obtained through PCA which combines the most significant information of the three RGB components. Secondly, several operations based on mathematical morphology are implemented with the aim of locating the OD. For that purpose, both stochastic and stratified watershed as well as geodesic transformation have been used. The algorithm has been validated on 5 different public databases obtaining promising results and improving the results of other methods of the literature.

The final goal of the proposed method is to make easier the early detection of diseases related to the fundus. Its main advantage is the full automation of the algorithm since it does not require any intervention by clinicians, which releases necessary resources (specialists) and reduces the consultation time, hence its use in primary care is facilitated.

As for future lines, the optic cup will also be detected with the goal of measuring the cup-to-disc (C/D) ratio. A high C/D ratio will indicate that a fundus is suspicious of glaucoma.

Acknowledgment

This work has been funded by the project IMIDTA/2010/47 and partially by projects Consolider-C (SEJ2006-14301/PSIC), "CIBER of Physiopathology of Obesity and Nutrition, an initiative of ISCIII" and Excellence Research Program PROMETEO (Generalitat Valenciana. Conselleria de Educación, 2008-157).

The authors would like to thank people who provide the public databases used in this work (DRIONS, DIARETDB1, DRIVE, MESSIDOR, and ONHSD). We want also to express our deep gratitude to Daniel Welfer for its collaboration and for letting us compare our results with his reference images, as well as to Arturo Aquino and Andrew Hunter for facilitating the access to their generated hand segmentations of the MESSIDOR database and to the ONHSD dataset, respectively.

References

[1] D. Pascolini and S. P. Mariotti, "Global estimates of visual impairment: 2010," *British Journal of Ophthalmology*, 2011.

[2] World Health Organization, *Action plan for the prevention of blindness and visual impairment, 2009-2013*. World Health Organization, 2010.

[3] H. R. Taylor, "Eye care for the community," *Clinical and Experimental Ophthalmology*, vol. 30, no. 3, pp. 151–154, 2002.

[4] T. Walter, J. C. Klein, P. Massin, and A. Erginay, "A contribution of image processing to the diagnosis of diabetic retinopathy-detection of exudates in color fundus images of the human retina," *Medical Imaging, IEEE Transactions on*, vol. 21, no. 10, pp. 1236–1243, 2002.

[5] L. D. Hubbard, R. J. Brothers, W. N. King, L. X. Clegg, R. Klein, L. S. Cooper, A. Sharrett, M. D. Davis, and J. Cai, "Methods for evaluation of retinal microvascular abnormalities associated with hypertension/sclerosis in the atherosclerosis risk in communities study," *Ophthalmology*, vol. 106, no. 12, pp. 2269 – 2280, 1999.

[6] M. D. Knudtson, K. E. Lee, L. D. Hubbard, T. Y. Y. Wong, R. Klein, and B. E. Klein, "Revised formulas for summarizing retinal vessel diameters." *Current Eye Research*, vol. 27, no. 3, pp. 143–149, Sep. 2003.

[7] J. Liu, D. W. K. Wong, J. H. Lim, H. Li, N. M. Tan, Z. Zhang, T. Y. Wong, and R. Lavanya, "Argali: An automatic cup-to-disc ratio measurement system for glaucoma analysis using level-set image processing," in *13th International Conference on Biomedical Engineering*, ser. IFMBE Proceedings. Springer Berlin Heidelberg, 2009, vol. 23, pp. 559–562.

[8] Y. Hatanaka, A. Noudo, C. Muramatsu, A. Sawada, T. Hara, T. Yamamoto, and H. Fujita, "Automatic measurement of vertical cup-to-disc ratio on retinal fundus images," in *Medical Biometrics*, ser. Lecture Notes in Computer Science. Springer Berlin / Heidelberg, 2010, vol. 6165, pp. 64–72.

[9] M. Niemeijer, M. D. A. moff, and B. van Ginneken, "Fast detection of the optic disc and fovea in color fundus photographs," *Medical Image Analysis*, vol. 13, no. 6, pp. 859 – 870, 2009.

[10] L. Gagnon, M. Lalonde, M. Beaulieu, and M. C. Boucher, "Procedure to detect anatomical structures in optical fundus images," *Proceedings of SPIE*, vol. 4322, pp. 1218–1225, 2001.

[11] M. Park, J. S. Jin, and S. Luo, "Locating the optic disc in retinal images," in *Proceedings of the International Conference on Computer Graphics, Imaging and Visualisation*. IEEE Computer Society, 2006, pp. 141–145.

[12] A. Aquino, M. E. Gegúndez-Arias, and D. Marín, "Detecting the optic disc boundary in digital fundus images using morphological, edge detection, and feature extraction techniques," *Medical Imaging, IEEE Transactions on*, vol. 29, no. 11, pp. 1860 –1869, nov. 2010.

[13] M. Lalonde, M. Beaulieu, and L. Gagnon, "Fast and robust optic disc detection using pyramidal decomposition and hausdorff-based template matching," *Medical Imaging, IEEE Transactions on*, vol. 20, no. 11, pp. 1193 –1200, nov. 2001.

[14] T. Kauppi and H. Kälviäinen, "Simple and robust optic disc localisation using colour decorrelated templates," in *Proceedings of the 10th International Conference on Advanced Concepts for Intelligent Vision Systems*, ser. ACIVS '08. Berlin, Heidelberg: Springer-Verlag, 2008, pp. 719–729.

[15] A. Osareh, M. Mirmehdi, B. Thomas, and R. Markham, "Comparison of colour spaces for optic disc localisation in retinal images," in *Pattern Recognition, 2002. Proceedings. 16th International Conference on*, vol. 1, 2002, pp. 743 – 746 vol.1.

[16] H. Li and O. Chutatape, "Automated feature extraction in color retinal images by a model based approach," *Biomedical Engineering, IEEE Transactions on*, vol. 51, no. 2, pp. 246 –254, 2004.

[17] J. Lowell, A. Hunter, D. Steel, A. Basu, R. Ryder, E. Fletcher, and L. Kennedy, "Optic nerve head segmentation." *IEEE Trans. Med. Imaging*, vol. 23, no. 2, pp. 256–264, 2004.

[18] J. Xu, O. Chutatape, E. Sung, C. Zheng, and P. Chew Tec Kuan, "Optic disk feature extraction via modified deformable model technique for glaucoma analysis," *Pattern Recognition*, vol. 40, pp. 2063–2076, July 2007.

[19] C. Eswaran, A. Reza, and S. Hati, "Extraction of the contours of optic disc and exudates based on marker-controlled watershed segmentation," in *Computer Science and Information Technology, 2008. ICCSIT '08. International Conference on*, 2008, pp. 719 –723.

[20] D. Welfer, J. Scharcanski, C. M. Kitamura, M. M. D. Pizzol, L. W. Ludwig, and D. R. Marinho, "Segmentation of the optic disk in color eye fundus images using an adaptive morphological approach," *Computers in Biology and Medicine*, vol. 40, no. 2, pp. 124 – 137, 2010.

[21] R. C. Gonzalez, R. E. Woods, and S. L. Eddins, *Digital Image Processing using MATLAB*. Pearson Prentice Hall, 2004.

[22] J. Hajer, H. Kamel, and E. Noureddine, "Localization of the optic disk in retinal image using the "watersnake"," in *Computer and Communication Engineering, 2008. ICCCE 2008. International Conference on*, 2008, pp. 947 –951.

[23] R. J. Qureshi, L. Kovacs, B. Harangi, B. Nagy, T. Peto, and A. Hajdu, "Combining algorithms for automatic detection of optic disc and macula in fundus images," *Computer Vision and Image Understanding*, vol. 116, no. 1, pp. 138 – 145, 2012.

[24] A. Hoover and M. Goldbaum, "Locating the optic nerve in a retinal image using the fuzzy convergence of the blood vessels," *Medical Imaging, IEEE Transactions on*, vol. 22, no. 8, pp. 951 –958, 2003.

[25] M. Foracchia, E. Grisan, and A. Ruggeri, "Detection of optic disc in retinal images by means of a geometrical model of vessel structure," *Medical Imaging, IEEE Transactions on*, vol. 23, no. 10, pp. 1189 – 1195, 2004.

[26] A.-H. Abdel-Razik Youssif, A. Ghalwash, and A. Abdel-Rahman Ghoneim, "Optic disc detection from normalized digital fundus images by means of a vessels' direction matched filter," *Medical Imaging, IEEE Transactions on*, vol. 27, no. 1, pp. 11 –18, 2008.

[27] I. T. Jolliffe, *Principal Component Analysis*, 2nd ed. Springer, 2002.

[28] J. C. Russ, *Image Processing Handbook*, 5th ed. CRC Press, Inc., 2007.

[29] M. Bertalmio, G. Sapiro, V. Caselles, and C. Ballester, "Image inpainting," in *Proceedings of the 27th annual conference on Computer graphics and interactive techniques*, ser. SIGGRAPH '00. ACM Press/Addison-Wesley Publishing Co., 2000, pp. 417–424.

[30] J. Serra, *Image Analysis and Mathematical Morphology*. London: Ac. Press, 1982, vol. I.

[31] L. Vincent, "Minimal path algorithms for the robust detection of linear features in gray images," in *Proceedings of the fourth international symposium on Mathematical morphology and its applications to image and signal processing*, ser. ISMM '98, 1998, pp. 331–338.

[32] A. Rosenfeld and J. L. Pfaltz, "Distance functions on digital pictures," *Pattern Recognition*, vol. 1, no. 1, pp. 33–61, 1968.

[33] S. Beucher and F. Meyer, *Mathematical Morphology in Image Processing*. E. Dougherty Ed., 1992.

[34] J. Angulo and D. Jeulin, "Stochastic watershed segmentation," in *Proc. of the 8th International Symposium on MathematicalMorphology (ISMM'2007)*, 2007, pp. 265–279.

[35] R. O. Duda and P. E. Hart, *Pattern Classification and Scene Analysis*. John Wiley & Sons Inc, 1973.

[36] J. B. MacQueen, "Some methods for classification and analysis of multivariate observations," in *Proc. of the fifth Berkeley Symposium on Mathematical Statistics and Probability*, vol. 1, 1967, pp. 281–297.

[37] T. Y. Wong, M. D. Knudtson, R. Klein, B. E. K. Klein, S. M. Meuer, and L. D. Hubbard, "Computer-assisted measurement of retinal vessel diameters in the beaver dam eye study: methodology, correlation between eyes, and effect of refractive errors." *Ophthalmology*, vol. 111, no. 6, pp. 1183–1190, 2004.

[38] C. A. Corral and C. S. Lindquist, "On implementing kasa's circle fit procedure," *IEEE Transactions on Instrumentation and Measurement*, vol. 47, no. 3, pp. 789–795, Jun. 1998.

[39] E. J. Carmona, M. Rincón, J. García-Feijoó, and J. M. Martínez-de-la-Casa, "Identification of the optic nerve head with genetic algorithms," *Artif. Intell. Med.*, vol. 43, pp. 243–259, July 2008.

[40] T. Kauppi, V. Kalesnykiene, J.-K. Kamarainen, L. Lensu, I. Sorri, A. A. Raninen, R. Voutilainen, H. Uusitalo, H. Kälviäinen, and J. Pietilä, "The DIARETDB1 diabetic retinopathy database and evaluation protocol," in *British Machine Vision Conference (BMVC2007)*, 2007, pp. 252–261.

[41] J. Staal, M. Abramoff, M. Niemeijer, M. Viergever, and B. van Ginneken, "Ridge-based vessel segmentation in color images of the retina," *Medical Imaging, IEEE Transactions on*, vol. 23, no. 4, pp. 501 –509, april 2004.

[42] Messidor Techno-Vision Project, "MESSIDOR: Digital retinal images," France, 2008, http://messidor.crihan.fr/download-en.php. Last access on 24th September, 2012.

[43] Retinal Image Computing & Understanding, "ONHSD - Optic Nerve Head Segmentation Dataset," University of Lincoln, United Kingdom, 2004, http://reviewdb.lincoln.ac.uk/Image Datasets/ONHSD.aspx. Last access on 24th September, 2012.

[44] V. Chalana, D. T. Linker, D. R. Haynor, and Y. Kim, "A multiple active contour model for cardiac boundary detection on echocardiographic sequences," *IEEE Transactions on Medical Imaging*, vol. 15, no. 3, pp. 290–298, Jun. 1996.

[45] "Expert system for early automated detection of dr by analysis of digital retinal images project website." Univ. Huelva, Spain, http://www.uhu.es/retinopathy/muestras.php. Last access on 24th September, 2012.

[46] S. Lu, "Accurate and efficient optic disc detection and segmentation by a circular transformation," *Medical Imaging, IEEE Transactions on*, vol. 30, no. 12, pp. 2126 –2133, 2011.